Chapter 2

Kinematics of massive star-forming cores: a JCMT study of infall, outflows, rotation, and turbulence

K.-S. Wang, M. R. Hogerheijde, F. F. S. van der Tak, and P. D. Klaassen
in preparation for journal submission

Abstract

Context. Like low-mass stars, massive stars may form via disk accretion, although more observational evidence is required to assess how general this phenomenon is.
Aims. Molecules like $C^{17}O$, $C^{34}S$, and CH_3CN are claimed in the literature to trace disks around massive protostars, based on interferometric data. We aim to establish if the these species are indeed robust tracers of disks.
Methods. We obtain single-dish observations with the James Clerk Maxwell Telescope toward 17 massive star-forming cores in lines of $C^{17}O$, $C^{34}S$, and CH_3CN near 345 GHz. We compare the line profiles to radiative transfer models that include rotation, infall, and turbulence.
Results. The $C^{17}O$ 3–2 emission toward all sources is extended in the $2' \times 2'$ maps, while $C^{34}S$ 7–6 and CH_3CN 18–17 lines remain largely unresolved in the $14''$ beam. Three different types of $C^{17}O$ 3–2 line profiles are found: single Gaussian, narrow+broad Gaussians, and two Gaussians with comparable FWHM. The $C^{34}S$ 7–6 and CH_3CN 18–17 lines are mostly single-peaked and Gaussian-like. The broad component of $C^{17}O$ 3–2 (FWHM linewidths $\sim$ 3.5–9.0 km s^{-1}) likely traces outflow activity, judging from the distribution of the high velocity gas. We speculate that the small observed linewidths of $C^{17}O$ (narrow components: 2.5 ± 0.7 km s^{-1}) and $C^{34}S$ (3.5 ± 0.7 km s^{-1}) sets an upper limit to the strength of turbulence at scales of a few 10,000 AU to a few 1000 AU, respectively. From the narrow $C^{34}S$ lines we find that the core's density profile is likely flatter than the assumed $\propto r^{-1.5}$ power-law. The broader CH_3CN lines

(6.5 ± 1.8 km s^{-1}) hint at infalling motions, or more likely, rotation, on scales below $\sim$ 1000 AU. Further detailed modeling of individual cores is required to confirm this result.

Conclusions. Our observations and comparisons to models suggest that $C^{17}O$ 3–2 and $C^{34}S$ 7–6 are good tracers of turbulence on scales of 10,000-1000 AU in massive star forming cores, while the broader CH_3CN 18–17 lines are promising tracers of rotation on $\lesssim$ 1000 AU scales for our entire sample. Turbulent motions may increase toward smaller radii inside these cores.

2.1 Introduction

Compared to Solar-type stars, the formation of massive stars ($M_\star \geq 8\ M_\odot$) is less understood both observationally and theoretically (Beuther et al. 2007; Zinnecker & Yorke 2007; McKee & Ostriker 2007). It is challenging to observe high-mass young stellar objects (YSOs) because they are rare and usually form in groups at large distances (typically a few kpc). More significantly, their formation occurs in much denser regions with high extinction, where only radiation at radio, (sub)millimeter and far-infrared wavelengths can escape. A key difference with low-mass star formation is that massive stars initiate hydrogen fusion while still accreting mass from their surroundings (Palla & Stahler 1993). The resulting large luminosities ($\sim 10^{3-5}\ L_\odot$), especially in the ultraviolet, affects the infalling material, ionizes the gas, and disrupts continued accretion. This interaction makes it much more difficult to unambiguously follow the formation process of massive stars, while, at the same time, the energetic feedback may play a fundamental role in regulating or shutting off the accretion. To understand massive star formation it is therefore essential to study the kinematics of massive star-forming cores, which provides clues on how massive stars accumulate their final mass.

Infall motions toward massive star-forming cores have been observed at both single-dish and interferometric scales in varies molecular lines at centimeter and (sub)millimeter wavelengths, such as ^{13}CO, $C^{18}O$, CS, NH_3, HCO^+ and HCN, etc. (e.g., Beltrán et al. 2006; Birkmann et al. 2007; Klaassen & Wilson 2007, 2008; Furuya et al. 2011; Liu et al. 2011a,b; Wyrowski et al. 2012; Rygl et al. 2013). The observed optically-thick line signatures such as the 'blue-skewed' line profiles and the inverse P-Cygni profiles provide supporting evidences for infall motions (Myers et al. 1996; Evans 1999). Outflow motions, usually observed in CO lines, are also ubiquitous in massive star-forming cores (e.g., Zhang et al. 2001; Beuther et al. 2002; López-Sepulcre et al. 2009, 2011), which provide an efficient way to remove the excess of angular momentum of an accreting star (Arce et al. 2007), and also provide a channel to re-direct strong radiation

pressure from massive stars (e.g., Krumholz et al. 2005).

Due to conservation of angular momentum, a flattened rotating structure, perhaps a circumstellar disk, should form around a young star with large scale infall motions (Ulrich 1976; Terebey et al. 1984). The high detection rates of bipolar outflows toward massive star-formimg cores (e.g., Zhang et al. 2001; Beuther et al. 2002) imply that disk-like structures around forming massive stars should be present, similar to the standard disk-outflow geometry observed in low-mass star-forming cores (Shu et al. 1987). However, to date, the presence of circumstellar "disks" is reported only toward few tens of young early B-type stars in a variety of tracers like radio (sub)millimeter emission lines (such as $C^{17}O$, $C^{34}S$, HDO, $H_2{}^{18}O$, $H^{13}CN$, $H^{13}CO^+$, NH_3, and CH_3CN) as well as infrared lines and polarization measurements (e.g., Cesaroni et al. 2007, and reference therein). These "disk-like" structures are found to be large ($\sim 10^{2-4}$ AU) and massive ($M_{\rm disk} \leq M_\star$), which is quite different from the disks around low-mass stars ($M_{\rm disk} \ll M_\star$). On the contrary, only large "toroids" undergoing solid-body rotation with masses greater than stellar masses are found toward young O-type stars (Beltrán et al. 2005; Furuya et al. 2008). Although not yet statistically significant, it seems that the formation of massive stars through disk accretion could be applied up to early B-type star as predicted in turbulent core accretion models (e.g., McKee & Tan 2003; Krumholz et al. 2009). However, the formation of O-type stars may follow different scenarios such as competitive accretion in clustered environment (e.g., Bonnell et al. 2001). As a result, studying the physical properties of these disks/toroids is an important step toward understanding the mass transport from envelopes to forming massive stars.

From (sub)millimeter interferometric observations, a collection of "disk" molecular line tracers can be made as listed above. An intermediate question one may ask is whether one disk tracer applicable to a certain source can also be applied to other sources for disk identification? We note that interferometric observations have spatial filtering effects which on the one hand are helpful for disk hunting, but on the other hand miss the large scale structure where infall and outflow happen, preventing us from making unambiguous disk identifications. In addition, the strong turbulence (typical FWHM $\geq 2-3$ km s^{-1}) toward massive star-forming cores makes the interpretations of kinematics even more difficult.

To investigate these issues, we initiated a survey of 17 massive star-forming cores in the $C^{17}O$ 3–2, $C^{34}S$ 7–6, and CH_3CN 18–17 lines with the James Clerk Maxwell Telescope[1] (JCMT). The selection of the first nine sources in our sample is based on the literature which reports possible detections of massive circumstellar disks through millimeter interferometric observations and infrared

[1]The James Clerk Maxwell Telescope is operated by the Joint Astronomy Centre on behalf of the Science and Technology Facilities Council of the United Kingdom, the National Research Council of Canada, and (until 31 March 2013) the Netherlands Organisation for Scientific Research.

observations. The other eight sources are selected based on the survey by Sridharan et al. (2002) and Beuther et al. (2002), which satisfy the following criteria: (1) weak centimeter-wave emission and strong millimeter-wave emission (ensuring the source is less evolved with no or little hot ionized gas), (2) presence of line wings and SiO emission (as the indication of outflow/shock gas, implying the potential existence of disk predicted by theoretical models), (3) presence of CH_3OH, CS and CH_3CN emission (tracing warm and compact molecular gas), and (4) kinematic distance less than 5 kpc. The basic characteristics of the selected sources are summarized in Table 2.1. The potentially optically thin $C^{17}O$ 3–2 and $C^{34}S$ 7–6 lines allow us to probe deeper into star-forming cores, while the highly excited CH_3CN 18–17 lines can trace the densest and warmest central regions of star-forming cores. The spectroscopic properties of the observed lines are summarized in Table 2.2. We aim to test if these lines are really promising as tracers of rotation and to see what the effect of turbulence is in the interpretation of the kinematics of massive star-forming cores including infall, outflows, and rotation.

We organize this paper as follows. In Sect. 2.2, we describe the JCMT observations and data reduction. In Sect. 2.3, we present the molecular images and spectra of our JCMT observations. Followed by molecular excitation and kinematics analysis in Sect. 2.4, we provide a general discussion of the kinematics in massive star-forming cores in Sect. 2.5. We conclude this paper in Sect. 2.6.

2.2 Observations and data reduction

The survey observations were taken with the 16-element Heterodyne Array Receiver Programme B (HARP–B[2]) and the Auto-Correlation Spectral Imaging System (ACSIS) correlator at the JCMT on the summit of Mauna Kea, Hawaii (Buckle et al. 2009). The 16 receptors of the HARP receiver are distributed in a 4×4 pattern with regular separations of $30''$. The survey was conducted in three semesters from 2009 to 2011 (Table 2.3).

In 2009 (project ID: M09BN07) and 2010 (M10BN06), we observed all 17 sources (Table 2.1) in $C^{17}O$ 3–2, $C^{34}S$ 7–6, and CH_3CN 18–17 (Table 2.2) with HARP–B in jiggle-chop mapping mode. The spectrometer was configured to operate in single sideband (SSB) mode with 250 MHz bandwidth to observe $C^{17}O$ 3–2 and $C^{34}S$ 7–6 simultaneously. The jiggle pattern of HARP4 was adopted to image a $\sim 2' \times 2'$ region with a pixel size of $7.5''$ which slightly under-samples the beam ($\sim 14''$). In the 2009 run, the integration time per jiggle position was 40 seconds, resulting a total observing time per source per line of ~ 90 minutes. In the 2010 run, the integration time per jiggle position was 34 seconds, result-

[2]http://www.jach.hawaii.edu/JCMT/spectral_line/Instrument_homes/HARP/HARP.html

Table 2.1. List of sample sources

Source	RA(J2000) (hh:mm:ss.s)	Dec(J2000) (dd:mm:ss)	d^a (kpc)	L^b ($L_\odot$)	$V_{\rm LSR}{}^c$ (km s^{-1})
AFGL 490	03:27:38.4	+58:47:04	1.0	2.0×10^3	−13.0
05358+3543	05:39:10.4	+35:45:19	1.8	6.3×10^3	−17.6
05553+1631	05:58:13.9	+16:32:00	2.5	6.3×10^3	+5.7
S255IR	06:12:54.0	+17:59:23	1.6	2.0×10^4	+7.0
18089−1732	18:11:51.3	−17:31:29	3.6	3.2×10^4	+34.0
18151−1208	18:17:57.1	−12:07:22	3.0	2.0×10^4	+32.8
18182−1433	18:21:07.9	−14:31:53	4.5	2.0×10^4	+59.1
18264−1152	18:29:14.3	−11:50:26	3.5	1.0×10^4	+43.6
19410+2336	19:43:11.4	+23:44:06	2.1	1.0×10^4	+22.4
20126+4104	20:14:25.1	+41:13:32	1.7	1.0×10^4	−4.0
AFGL 2591	20:29:24.9	+40:11:21	3.3	2.2×10^5	−6.0
20293+3952	20:31:10.7	+40:03:10	2.0	6.3×10^3	+6.3
S140 IRS1	22:19:18.2	+63:18:47	0.8	8.5×10^3	−7.0
Cepheus A	22:56:17.9	+62:01:49	0.7	2.5×10^4	−3.0
23033+5951	23:05:24.8	+60:08:14	3.5	1.0×10^4	−53.0
NGC 7538S	23:13:44.8	+61:26:51	2.7	1.5×10^4	−56.0
23139+5939	23:16:09.3	+59:55:23	4.8	2.5×10^4	−44.7

Note. — [a]Distance. [b]Bolometric luminosity. [c]LSR velocity.

Table 2.2. List of observed molecular lines

Molecule	Transition	Frequency (MHz)	$E_{\rm u}{}^a$ (K)	$n_{\rm crit}{}^b$ (cm^{-3})
$C^{17}O$	3–2	337061.1	32	3.4×10^4
$C^{34}S$	7–6	337396.5	65	1.9×10^7
CH_3CN	18_0–17_0	331071.5	151	1.5×10^7
	18_1–17_1	331065.2	158	1.4×10^7
	18_2–17_2	331046.1	180	1.4×10^7
	18_3–17_3	331014.3	215	1.5×10^7
	18_4–17_4	330969.8	265	1.5×10^7
	18_5–17_5	330912.6	329	1.4×10^7
	18_6–17_6	330842.8	408	1.4×10^7
	18_7–17_7	330760.3	501	1.4×10^7

Note. — [a]Upper level energy. [b]Critical density at 100 K, derived using collisional rate coefficients from Yang et al. (2010), Turner et al. (1992), Green (1986), as summarized by Schöier et al. (2005).

Table 2.3. Summary of the JCMT observations

	M09BN07	M10BN06	M11BN08
Target line	$C^{17}O$ 3–2 $C^{34}S$ 7–6 CH_3CN 18–17	$C^{17}O$ 3–2 $C^{34}S$ 7–6 CH_3CN 18–17	CH_3CN 18–17
Bandwidth	250 MHz	250 MHz	1000 MHz
Observing mode	Mapping Jiggle-chop	Mapping Jiggle-chop	Stare
Observing time[a]	90 mins	60 mins	75 mins
Typical $\tau_{225\mathrm{GHz}}$	0.05–0.08	0.05–0.08	0.08–0.12
Target source	AFGL 490 S255IR 18089−1732 20126+4104 AFGL 2591 Cepheus A 23033+5951 NGC 7538S	05358+3543 05553+1631 18151−1208 18182−1433 18264−1152 19410+2336 20293+3952 S140 IRS1 23139+5939	AFGL 490 05358+3543 05553+1631 S255IR 19410+2336 20126+4104 20293+3952 S140 IRS1 23033+5951 NGC 7538S 23139+5939

Note. — The CH_3CN 18–17 single pointing spectrum of IRAS 18089−1732 is taken from the JCMT archive with project code M09BN10 (Isokoski et al. 2013). [a]Observing time per source per line.

ing a total observing time per source per line of $\sim$ 60 minutes. In the 2011 run (M11BN08), we observed 11 sources in CH_3CN 18–17 with HARP–B in single pointing mode for better signal-to-noise (S/N) ratio. The spectrometer was configured to operate in SSB mode with 1000 MHz bandwidth. The integration time was 450 seconds per offset position and the total observing time per source was $\sim$75 minutes. The typical atmospheric opacities at 225 GHz in 2009/2010 and 2011 were 0.05–0.08 and 0.08–0.12, respectively. In all observing runs, the receptor R15 (H14) was offline, resulting a $30'' \times 30''$ blank area in final images.

The raw time-series data are processed with the Starlink[3] software package. Each scan is inspected for bad receptors, baseline issues, and spikes, which are flagged out before time summation and transforming into image cubes. Baselines are removed by selecting line-free channels as reference. The intensity is scaled from the corrected antenna temperature T_{A}^{*} to the main beam temperature

[3]http://starlink.jach.hawaii.edu/starlink

$T_{\rm MB}$ by adopting a main beam efficiency of 0.61 ± 0.03 (Buckle et al. 2009). The final calibrated image cubes were exported to FITS file and we use the MIRIAD software package (Sault et al. 1995) for further analysis. A Gaussian-like emission spike close to the K=2 transition was found in the CH_3CN 18–17 spectrum, which is a ghost signal from the receptor R06 (H05). Therefore, we did not use the K=2 transition for further analysis.

In addition to the line observations, we obtained the SCUBA 850 μm images from the database presented by Di Francesco et al. (2008). The images are regridded to match the pixel size of line images ($7.5''$). The 850 μm image of IRAS 20293+3952 is partly corrupted.

2.3 Results

2.3.1 Molecular distribution

In Fig. 2.1, we present the integrated intensity maps of $C^{17}O$ 3–2 (blue contours) and $C^{34}S$ 7–6 (yellow contours) toward all 17 sources. The SCUBA 850 μm continuum emission (peak intensity is normalized to unity) taken from the archive published by Di Francesco et al. (2008) is also shown in grey scale. In all cases except IRAS 05358+3543, the $C^{17}O$ 3–2 emission peak (S/N $>$ 10) is spatially correlated with the 850 μm continuum peak, suggesting that gas and dust are coupled well at core scales (a few 0.1 pc). The "Main" source toward IRAS 05358+3543 shows stronger 850 μm emission and weaker $C^{17}O$ 3–2 emission, while the "SW" source behaves in the opposite way. Toward all 17 sources, $C^{34}S$ 7–6 emission is detected, which is also spatially correlated with the 850 μm emission. The $C^{34}S$ 7–6 emission is more compact than the $C^{17}O$ 3–2 emission, likely because $C^{34}S$ 7–6 requires much higher gas densities than $C^{17}O$ 3–2 for collisional excitation (Table 2.2). The different excitation conditions and the good spatial correlation with the 850 μm emission make $C^{17}O$ 3–2 and $C^{34}S$ 7–6 good tracers of gas kinematics from the large envelope to the central, dense part of star-forming cores.

Gaussian fits are performed to further study the morphology of the extended $C^{17}O$ 3–2 emission and the SCUBA 850 μm continuum. In Fig. 2.1, the $C^{17}O$ 3–2 emission shows the complex morphologies in our sample, such as elongated (e.g., AFGL 490), compact (e.g., IRAS 05553+1631), and multiple-core (e.g., IRAS 05358+3543). To have a rough estimate of emission sizes, we assume that the emission can be approximated as a single elliptical Gaussian peaking at emission peak (i.e., the center position is fixed in the fit). We note that the fit may be affected by the boundary of our maps ($\sim 2' \times 2'$) and the presence of multiple local emission peaks. The purpose here is to have an idea of the differences of the spatial distributions of $C^{17}O$ 3–2 and 850 μm continuum at a few 0.1 pc scales. We fit all the $C^{17}O$ 3–2 and 850 μm continuum maps and

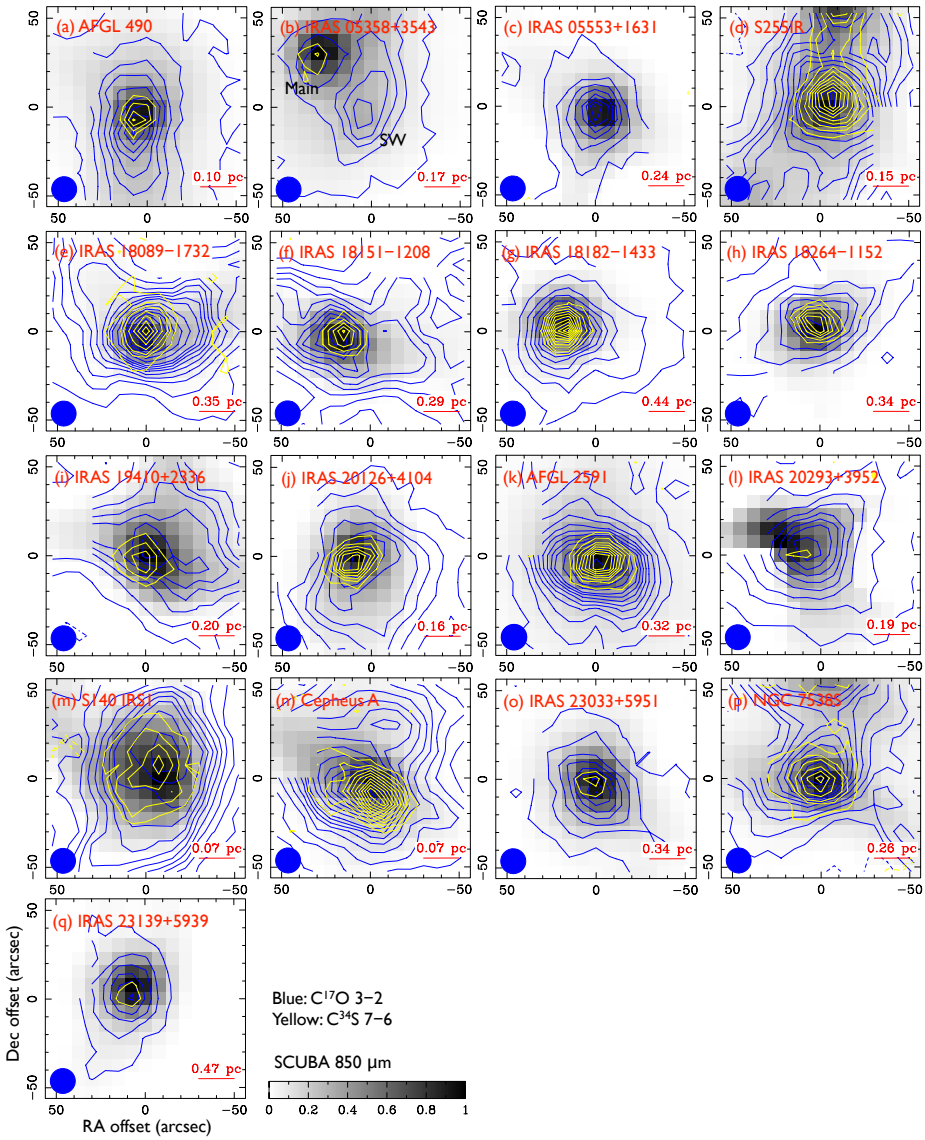

Figure 2.1 Integrated intensity maps ($\int T_{\rm MB} dV$) of $C^{17}O$ 3–2 (blue contours) and $C^{34}S$ 7–6 (yellow contours) toward our sample massive star-forming cores. The image in grey is the SCUBA 850 μm emission (peak intensity is normalized to unity) taken from Di Francesco et al. (2008). The blue circle represents the $\sim 14''$ resolution of the JCMT HARP–B observations. The bar in red gives the linear scale in pc. The (0,0) position of each map is our pointing center and its absolute coordinate is given in Table 2.1. The 1-σ noise levels of $C^{17}O$ 3–2 from panel (a) to (q) are 0.14, 0.14, 0.15, 0.11, 0.15, 0.14, 0.18, 0.16, 0.14, 0.12, 0.14, 0.14, 0.19, 0.18, 0.13, 0.14, and 0.17 K km s^{-1}. The contour levels of $C^{17}O$ in all panels are 3, 8, 13, ... , 43, 53, 63, ... σ. The 1-σ noise levels of $C^{34}S$ 7–6 from panel (a) to (q) are 0.09, 0.13, 0.15, 0.11, 0.18, 0.13, 0.22, 0.17, 0.11, 0.13, 0.11, 0.10, 0.17, 0.19, 0.12, 0.17, and 0.11 K km s^{-1}. The contour levels of $C^{34}S$ in all panels are 3, 5, 7, ... σ.

summarize the results in Table 2.4. We found that in all sources, the geometric mean sizes derived from the 850 μm continuum images are all smaller than the sizes derived from the $C^{17}O$ 3–2 images. Likely this is because $C^{17}O$ 3–2 partly traces outflows which would naturally enlarge the sizes of overall distributions (See Sect. 2.3.3), or because of the fact that $C^{17}O$ is more sensitive to lower density gas than the 850 μm continuum is. Therefore, we suggest that the effect of outflows in shaping the $C^{17}O$ 3–2 line profiles cannot be neglected in massive star-forming cores.

We tried to image CH_3CN 18–17 transitions in our sample but only AFGL 2591 and Cepheus A show detections with point source morphology (not shown here). A further attempt was made in single pointing mode to detect the lines. We expect the CH_3CN 18–17 emission to be point-source like in a $\sim 14''$ beam since it usually arises in a hot core of a few arcsecond in size. We present the CH_3CN 18–17 spectra in Sect. 2.3.2. Excitation analysis of CH_3CN lines and the determination of emission size are given in Sect. 2.4.1.

2.3.2 Molecular spectra

We present a collection of $C^{17}O$ 3–2 and $C^{34}S$ 7–6 spectra in Fig. 2.2. The beam-averaged spectra are taken at the emission peak based on the integrated intensity maps (Fig. 2.1). To enhance the S/N and minimize the effect of undersampling of HARP–B maps, we averaged 3×3 pixels ($22.5'' \times 22.5''$) centered at the emission peak to derive the spectra. The typical line profiles of $C^{17}O$ 3–2 and $C^{34}S$ 7–6 are Gaussian-like, suggesting that turbulence may dominate the kinematics of our source sample. Exceptions can be seen in $C^{34}S$ 7–6 toward IRAS 20126+4104 and Cepheus A, which shows double-peaked profiles. A detailed check of the high S/N ratio spectra of $C^{17}O$ 3–2 shows that some line profiles contain an additional broad component (FWHM linewidths $\sim$ 3.5–9.0 km s^{-1}) at low intensity level (e.g., IRAS 18264−1152 and IRAS 20126+4104). The presence of this broad low-level component implies that $C^{17}O$ 3–2 may trace part of outflow motions near the source.

We performed Gaussian fits to decompose different kinematical components and summarize the results in Table 2.5 and Fig. 2.2. We adopted a rule to determine the total number of Gaussian components in the decomposition process of a line profile. For a pure Gaussian line profile, the full width at p % of maximum intensity (ΔV_p) follows $\Delta V_p = 2 \times \mathrm{FWHM} \times \sqrt{\ln(p/100)/ - 4\ln 2}$. In other words, ΔV_{50} is exactly $\sqrt{1}\times$FWHM linewidth, ΔV_{25} is $\sqrt{2}\times$FWHM linewidth, and $\Delta V_{12.5}$ is $\sqrt{3}\times$FWHM linewidth, etc. This forms a very useful test to determine if the observed line profile is a single Gaussian or a superposition of multiple Gaussians. If there is a low-level emission line wing in the observed line profile, through a series of tests with different p, we can quantitatively determine how many Gaussians are needed to decompose the line

Table 2.4. Gaussian decomposed size of $C^{17}O$ 3–2 and SCUBA 850 μm emission

Source	$C^{17}O$ 3–2 Angular			$C^{17}O$ 3–2 Linear			850 μm Angular			850 μm Linear		
	θ_a ($''$)	θ_b ($''$)	P.A. ($^\circ$)	θ_a (pc)	θ_b (pc)	θ_{mean} (pc)	θ_a ($''$)	θ_b ($''$)	P.A. ($^\circ$)	θ_a (pc)	θ_b (pc)	θ_{mean} (pc)
AFGL 490	75	34	0	0.38	0.17	0.25	52	34	0	0.26	0.17	0.21
05358+3543	111	78	53	0.94	0.66	0.79	54	49	73	0.46	0.42	0.44
05553+1631	39	25	−5	0.47	0.30	0.37	29	25	−24	0.35	0.30	0.32
S255IR	106	48	−18	0.80	0.36	0.53	69	41	−22	0.52	0.31	0.40
18089−1732	46	33	90	0.81	0.58	0.68	31	23	−89	0.54	0.40	0.47
18151−1208	129	50	76	1.87	0.73	1.16	35	22	69	0.51	0.32	0.40
18182−1433	33	29	−77	0.73	0.64	0.68	26	22	−81	0.57	0.48	0.53
18264−1152	73	35	−58	1.24	0.60	0.86	28	21	−73	0.48	0.36	0.41
19410+2336	98	53	74	0.98	0.53	0.72	45	35	62	0.45	0.35	0.40
20126+4104	68	55	19	0.54	0.44	0.49	35	28	−11	0.28	0.22	0.25
AFGL 2591	43	30	76	0.69	0.48	0.57	46	36	50	0.74	0.58	0.65
20293+3952	59	49	−70	0.56	0.47	0.51	50	32	81	0.48	0.30	0.38
S140 IRS1	115	69	−29	0.40	0.24	0.31	52	44	49	0.18	0.15	0.17
Cepheus A	81	60	22	0.28	0.21	0.24	51	31	54	0.18	0.11	0.14
23033+5951	48	31	44	0.82	0.53	0.66	34	27	23	0.58	0.46	0.52
NGC 7538S	58	46	−56	0.75	0.60	0.67	43	35	79	0.56	0.46	0.50
23139+5939	36	25	−7	0.85	0.59	0.70	27	23	−32	0.63	0.54	0.59

Note. — The uncertainties in θ_a (major axis) and θ_b (minor axis) are all less than $7.5''$ (one pixel size). θ_{mean} is the geometric mean size. The uncertainty in source distance is not considered in converting angular size to linear size.

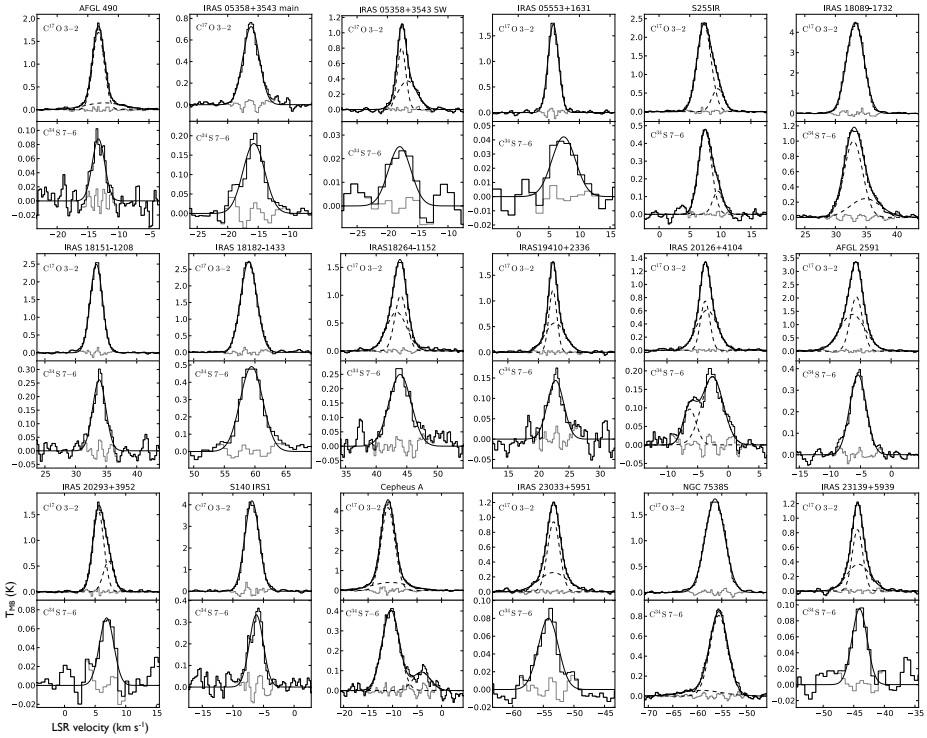

Figure 2.2 Beam-averaged $C^{17}O$ 3–2 and $C^{34}S$ 7–6 spectra taken at emission peaks of all sample sources. The observed spectra are plotted in black histogram. The Gaussian fit is plotted in solid lines, while each Gaussian component (if any) is shown in dashed lines. The fitting residual is plotted in grey histogram.

profile. We applied this test to the observed $C^{17}O$ 3–2 line profiles and allowed a 10% tolerance when comparing the apparent FWHM linewidth with the apparent ΔV_p. Through this analysis, the $C^{17}O$ 3–2 line profiles can be classified into three categories: single Gaussian (e.g., IRAS 05553+1631), narrow+broad Gaussians (e.g., IRAS 19410+2336), and two Gaussians with comparable FWHM linewidth (e.g., S255IR). Similar to $C^{17}O$ 3–2, the $C^{34}S$ 7–6 line profiles can also be classified in these three categories in spite of their lower S/N ratios.

Table 2.5. Beam-averaged line properties of $C^{17}O$ 3–2 and $C^{34}S$ 7–6

Source	W^a (K km s^{-1})	ΔV^b (km s^{-1})	$V_{\rm LSR}{}^c$ (km s^{-1})	Note
		$C^{17}O$ 3–2		
AFGL 490	4.02 ± 0.06	2.23 ± 0.02	-13.26 ± 0.01	Narrow component
	1.20 ± 0.07	7.48 ± 0.41	-12.28 ± 0.16	Broad component
05358+3543 Main	2.44 ± 0.15	3.16 ± 0.22	-16.15 ± 0.09	Single component
05358+3543 SW	1.42 ± 0.28	1.66 ± 0.16	-17.66 ± 0.05	Narrow component
	1.48 ± 0.29	3.72 ± 0.35	-16.71 ± 0.28	Broad component
05553+1631	3.73 ± 0.12	2.03 ± 0.07	5.73 ± 0.03	Single component
S255IR	6.76 ± 0.15	2.70 ± 0.04	7.35 ± 0.03	Component I
	1.48 ± 0.15	2.25 ± 0.10	9.60 ± 0.08	Component II
18089−1732	16.00 ± 0.05	3.34 ± 0.01	33.24 ± 0.01	Single component
18151−1208	6.25 ± 0.11	2.35 ± 0.05	33.40 ± 0.02	Single component
18182−1433	9.12 ± 0.13	3.13 ± 0.05	59.00 ± 0.02	Single component
18264−1152	2.40 ± 1.13	2.27 ± 0.34	44.01 ± 0.10	Narrow component
	2.89 ± 1.13	3.91 ± 0.42	43.34 ± 0.32	Broad component
19410+2336	1.97 ± 0.39	1.53 ± 0.15	22.36 ± 0.04	Narrow component
	2.37 ± 0.38	3.89 ± 0.47	22.70 ± 0.15	Broad component
20126+4104	1.43 ± 0.15	1.80 ± 0.07	-3.77 ± 0.02	Narrow component
	2.59 ± 0.14	3.99 ± 0.13	-3.46 ± 0.04	Broad component
AFGL 2591	5.12 ± 1.05	2.36 ± 0.19	-5.68 ± 0.05	Narrow component
	7.19 ± 1.04	4.88 ± 0.34	-6.33 ± 0.15	Broad component
20293+3952	3.60 ± 1.44	2.15 ± 0.36	5.53 ± 0.34	Component I
	1.30 ± 1.43	2.05 ± 0.83	7.20 ± 0.81	Component II
S140 IRS1	12.35 ± 0.10	2.74 ± 0.03	-6.88 ± 0.01	Single component
Cepheus A	14.42 ± 0.18	3.26 ± 0.02	-10.93 ± 0.01	Narrow component
	3.99 ± 0.18	9.23 ± 0.37	-10.43 ± 0.10	Broad component
23033+5951	2.35 ± 0.14	2.35 ± 0.06	-53.32 ± 0.01	Narrow component
	1.54 ± 0.14	5.61 ± 0.35	-53.38 ± 0.08	Broad component
NGC 7538S	9.08 ± 0.03	4.72 ± 0.02	-56.37 ± 0.01	Single component
23139+5939	1.83 ± 0.79	2.04 ± 0.35	-44.38 ± 0.07	Narrow component
	1.77 ± 0.76	4.51 ± 1.16	-44.23 ± 0.26	Broad component
		$C^{34}S$ 7–6		
AFGL 490	0.22 ± 0.02	2.40 ± 0.28	-13.25 ± 0.12	Single component
05358+3543 Main	0.80 ± 0.04	4.20 ± 0.24	-15.70 ± 0.10	Single component
05358+3543 SW	0.12 ± 0.03	4.36 ± 1.18	-17.97 ± 0.49	Single component
05553+1631	0.21 ± 0.04	4.58 ± 0.96	7.42 ± 0.41	Single component
S255IR	1.26 ± 0.12	2.50 ± 0.16	7.50 ± 0.11	Component I
	0.28 ± 0.12	2.05 ± 0.42	9.64 ± 0.30	Component II
18089−1732	3.75 ± 1.01	3.52 ± 0.30	32.94 ± 0.08	Component I*
	1.54 ± 1.03	5.87 ± 1.03	34.92 ± 1.45	Component II*
18151−1208	0.71 ± 0.16	2.53 ± 0.65	33.87 ± 0.28	Single component
18182−1433	2.28 ± 0.06	4.36 ± 0.14	59.45 ± 0.06	Single component
18264−1152	1.14 ± 0.25	4.29 ± 1.09	43.91 ± 0.47	Single component

Table 2.5 (cont'd)

Source	W^a (K km s^{-1})	ΔV^b (km s^{-1})	$V_{\rm LSR}{}^c$ (km s^{-1})	Note
19410+2336	0.48 ± 0.12	3.14 ± 0.94	22.80 ± 0.40	Single component
20126+4104	0.81 ± 0.07	4.12 ± 0.40	-2.57 ± 0.18	Component I*
	0.26 ± 0.07	2.54 ± 0.46	-6.29 ± 0.23	Component II*
AFGL 2591	1.26 ± 0.09	3.19 ± 0.27	-5.40 ± 0.12	Single component
20293+3952	0.21 ± 0.03	2.78 ± 0.46	6.88 ± 0.20	Single component
S140 IRS1	0.96 ± 0.15	2.69 ± 0.48	-6.17 ± 0.20	Single component
Cepheus A	0.41 ± 0.05	4.18 ± 0.59	-4.04 ± 0.23	Component I*
	1.79 ± 0.05	4.15 ± 0.14	-10.37 ± 0.05	Component II*
23033+5951	0.33 ± 0.03	3.85 ± 0.35	-54.17 ± 0.15	Single component
NGC 7538S	3.70 ± 0.13	4.31 ± 0.07	-55.59 ± 0.02	Component I*
	0.60 ± 0.14	9.85 ± 1.17	-59.20 ± 1.08	Component II*
23139+5939	0.30 ± 0.03	2.92 ± 0.32	-44.05 ± 0.14	Single component

Note. — Components with * listed in the $C^{34}S$ 7–6 part represent different gaussian fit compared to $C^{17}O$ 3–2 (See Fig. 2.2). [a]Beam-averaged integrated intensity: $W = \int T_{\rm MB} dV$, where $T_{\rm MB}$ is the main beam temperature. [b]Gaussian FWHM linewidth. [c]Gaussian line center LSR velocity.

Different kinematical components hidden in line profiles can be decomposed by multiple Gaussians as described above only if the line emission is optically thin. To quantify the opacities of the observed $C^{17}O$ 3–2 and $C^{34}S$ 7–6 lines, we use the Eq. (27) of Goldsmith & Langer (1999) as an estimate. Assuming an H_2 column density of 3×10^{23} cm^{-2} (c.f., Hatchell et al. 2000) and a Gaussian line profile with a FWHM linewidth of 4.0 km s^{-1}, the line center opacities of $C^{17}O$ 3–2 are ~ 0.5 and ~ 0.1 at 40 K and 100 K, respectively, if we adopt a fractional abundance of 1×10^{-7} as derived from Lacy et al. (1994) and Wilson & Rood (1994). The line center opacities of $C^{34}S$ 7–6 are ~ 0.2 and ~ 0.08 at 40 K and 100 K, respectively, assuming a fractional abundance of 3×10^{-10} based on van der Tak et al. (2000) and Wilson & Rood (1994). The real line opacities of the $C^{17}O$ 3–2 and $C^{34}S$ 7–6 lines of each source may vary by a factor of few, but in all cases we suggest that these two lines are optically thin and it is safe to perform line decompositions with Gaussians.

In Fig. 2.3, we present the 8 sources with detections of CH_3CN 18–17. Due to limited S/N, we do not apply the Gaussianity test outlined above. In deriving the line center velocity, FWHM linewidth, and integrated intensity, we assume that the line profile of each K component is Gaussian. We further assume that the FWHM linewidth and line center velocity of each K component are the same in the fitting process. For sources with low S/N, we fit their linewidth by eye and keep it fixed in the fit. We summarize the line properties of CH_3CN 18–17 in

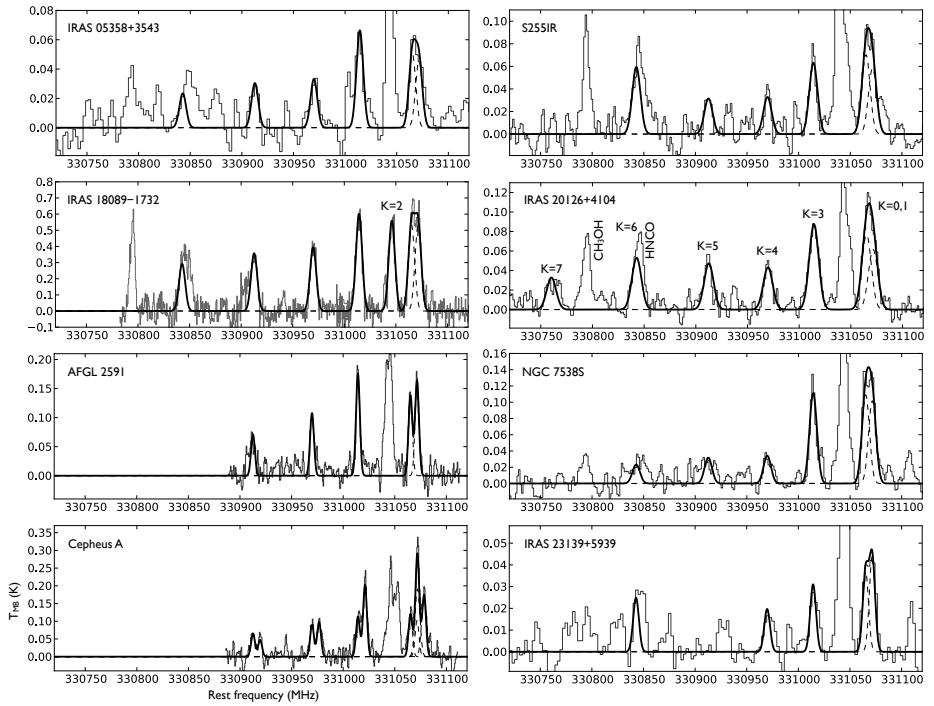

Figure 2.3 Beam-averaged CH_3CN 18–17 spectra toward 8 massive star-forming cores. The observed spectra are plotted in histogram, while the thick lines represent the best-fit spectra with each K component in dashed lines. We label the K components and other molecular lines in the panels of IRAS 18089−1732 and IRAS 20126+4104. The spectral feature near the $K = 2$ component of all sources except IRAS 18089−1732 is a superposition of the target signal and the ghost signal from receiver (See Sect. 2.2).

Table 2.6. Toward Cepheus A, the line profile of each K component is double-peaked, implying that likely there are two velocity components along the line of sight, also known from other species (e.g., CH_3OH; Torstensson et al. 2011). Therefore, we used two sets of Gaussians to decompose the observed spectrum. From the fit, the assumption of similar line center velocity and FWHM linewidth of all K components is valid.

Apparently, the observed linewidths of $C^{17}O$ 3–2, $C^{34}S$ 7–6 and CH_3CN 18–17 form an interesting sequence with $C^{17}O$ 3–2 the narrowest and CH_3CN 18–17 the broadest. To quantify this, we averaged the FWHM linewidth of the narrow component of all three lines. If the line profile is classified as two Gaussians with comparable FWHM, we use the strongest one. We note that the broad component seen in $C^{17}O$ 3–2 may come from outflow motions (see Sect. 2.3.3). As a result, we found that the mean FWHM linewidths are 2.5 ± 0.7 km s^{-1}, 3.5 ± 0.7 km s^{-1},

Table 2.6. Beam-averaged line properties of CH_3CN 18–17

	IRAS05358	S255IR	IRAS18089	IRAS20126	AFGL2591	NGC7538S	CepA–1	CepA–2	IRAS23139
$V_{\rm LSR}{}^a$	-16.5 ± 0.4	5.0 ± 0.4	33.4 ± 0.1	-4.3 ± 0.3	-5.1 ± 0.1	-56.4 ± 0.2	-4.4 ± 0.1	-10.6 ± 0.1	-42.6 ± 0.3
ΔV^b	7.0 (fixed)	8.5 ± 0.7	6.4 ± 0.2	9.7 ± 0.4	4.0 (fixed)	7.7 ± 0.4	4.0 (fixed)	5.0 (fixed)	6.0 ± 0.5
W^c									
$K = 0$	0.34 ± 0.07	0.53 ± 0.10	3.60 ± 0.20	0.64 ± 0.09	0.70 ± 0.03	0.83 ± 0.07	0.43 ± 0.21	0.93 ± 0.05	0.28 ± 0.04
$K = 1$	0.37 ± 0.07	0.63 ± 0.10	3.61 ± 0.20	0.79 ± 0.09	0.59 ± 0.03	0.89 ± 0.07	0.51 ± 0.04	1.02 ± 0.23	0.24 ± 0.04
$K = 2$	ghost	ghost	3.80 ± 0.19	ghost	ghost	ghost	ghost	ghost	ghost
$K = 3$	0.50 ± 0.06	0.57 ± 0.07	4.08 ± 0.19	0.91 ± 0.06	0.75 ± 0.03	0.91 ± 0.05	0.48 ± 0.04	1.08 ± 0.04	0.20 ± 0.04
$K = 4$	0.25 ± 0.06	0.30 ± 0.07	2.68 ± 0.19	0.45 ± 0.06	0.46 ± 0.03	0.28 ± 0.05	0.38 ± 0.04	0.52 ± 0.04	0.13 ± 0.04
$K = 5$	0.23 ± 0.06	0.28 ± 0.07	2.42 ± 0.19	0.49 ± 0.06	0.30 ± 0.03	0.26 ± 0.05	0.28 ± 0.04	0.25 ± 0.04	...
$K = 6$	0.17 ± 0.06	0.54 ± 0.10	1.98 ± 0.35	0.55 ± 0.12	...	0.19 ± 0.09	...		0.16 ± 0.05
$K = 7$	...	...	...	0.34 ± 0.06	...	...	...		...
δW^d	0.12	0.12	0.26	0.10	0.07	0.10	0.10	0.10	0.11
RADEX excitation analysis in LVG approximation^e									
$T_{\rm kin}{}^f$	200	240	110	370	180	110	80	140	130
$N_{\rm mol}{}^g$	7×10^{15}	5×10^{16}	2×10^{17}	3×10^{16}	2×10^{16}	3×10^{15}	2×10^{17}	4×10^{15}	5×10^{16}
$n(H_2)^h$	$\geq 10^6$	$\geq 10^6$	$\geq 10^6$	$\geq 10^6$	$\geq 10^6$	$\geq 10^6$	$\geq 10^6$	$\geq 10^6$	$\geq 10^6$
f^i	6.0×10^{-4}	6.0×10^{-4}	6.4×10^{-3}	4.0×10^{-4}	2.1×10^{-3}	2.5×10^{-3}	1.7×10^{-3}	2.7×10^{-3}	5.0×10^{-4}
$\theta_{\rm s}{}^i$	0.3	0.3	1.1	0.3	0.6	0.7	0.6	0.7	0.3
$\theta_{\rm s,linear}{}^i$	620	550	4000	480	2100	1900	400	510	1500

Note. — The $K = 2$ component of all listed sources except IRAS18089 has a ghost emission from the receptor. We do not derive the line properties of the $K = 2$ component. [a]LSR velocity in km s^{-1}. We assume that all K components have the same velocity in the Gaussian fitting process. [b]FWHM linewidth in km s^{-1}. We assume that all K components have the same linewidth in the Gaussian fitting process. [c]Integrated intensity in K km s^{-1}. [d]The 3-σ upper limit of the integrated intensity ($3 \times 1.064 \times \sigma\sqrt{\delta V \Delta V}$) in K km s^{-1}. [e]Only the best-fit solution is listed. The uncertainty of each free parameter is presented graphically in Fig. 2.9 and 2.10. [f]Kinetic temperature in K. [g]Total molecular column density in cm^{-2}. [h]H_2 volume density in cm^{-3}. A lower-limit value is listed since this parameter is less constrained (Fig. 2.9 and 2.10). [i]Assuming a Gaussian beam and a Gaussian source geometry, the filling factor f is $\theta_{\rm b}^2/(\theta_{\rm b}^2+\theta_{\rm s}^2)$, where $\theta_{\rm b}$ and $\theta_{\rm s}$ are the beam size and source size in arcsecond, respectively. The linear source size in AU $\theta_{\rm s,linear}$ is calculated by adopting the distance listed in Table 2.1.

and 6.5 ± 1.8 km s^{-1} for $C^{17}O$ 3–2, $C^{34}S$ 7–6 and CH_3CN 18–17, respectively. This result suggests that if turbulence dominates the observed line profiles, there should be a gradient in the strength of turbulence throughout the star forming core, with turbulence stronger close to the forming stars. However, it is also possible that the apparent larger mean FWHM linewidths seen in $C^{34}S$ 7–6 and CH_3CN 18–17 come from other kinematics such as infall and/or rotation, or interaction of outflows with dense inner envelopes, that are more pronounced at the smaller scales probed by these lines. We further investigate this aspect in Sect. 2.4.

2.3.3 Distributions of high-velocity gas

In the previous section, we found that line emission wings can be seen in the $C^{17}O$ 3–2 spectra toward some sources (Fig. 2.2). It is therefore interesting to investigate the spatial distributions of the high velocity gas traced by $C^{17}O$ 3–2. To do so, we use the spectra presented in Fig. 2.2 as the reference and integrate over the velocity ranges set by the 3-σ intensity and 50 % peak intensity. Results are plotted in red and blue contours in Fig. 2.4. We find that toward many sources, the apparent positional offsets in the peak positions of the blue- and red-shifted components imply that the high-velocity gas traced by $C^{17}O$ 3–2 likely follows outflow motions. It is possible that the apparent positional offset near the forming star is due to cloud rotation at ~ 0.1 pc scales. However, this would require a very large central stellar mass (violating the total luminosity) unless self-gravity of the entire core cannot be ignored. We suggest that the typical broad line component seen in $C^{17}O$ and other CO isotopologues in single-pointing single-dish observations is an indication of outflow motions. In later analysis (Sect. 2.4), we therefore focus on the narrow component and look for its origin.

2.4 Analysis

2.4.1 CH_3CN J=18–17 excitation analysis and emission size

For sources with multiple detections of the CH_3CN J=18–17 K components, we perform excitation analysis in order to study the physical conditions where CH_3CN originates. We use "rotation diagrams" (c.f., Turner 1991) to visualize the level populations derived from the observed line intensities (Table 2.6). In such plots, the natural logarithmic value of upper state column density ($N_{\rm u}$) per statistical weight ($g_{\rm u}$) calculated as

$$\ln(\frac{N_{\rm u}}{g_{\rm u}}) = \ln(\frac{3kW}{8\pi^3\nu S\mu^2 g_I g_K}), \tag{2.1}$$

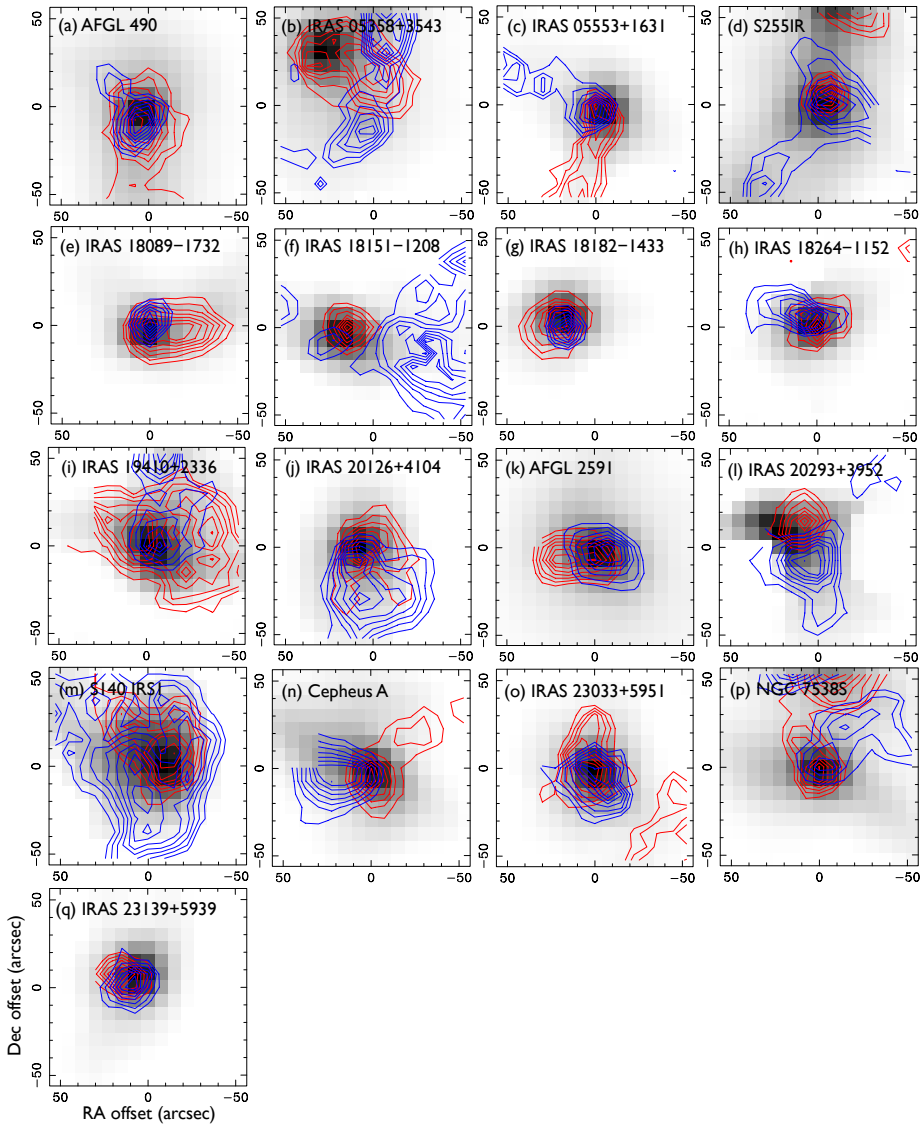

Figure 2.4 High-velocity gas traced by $C^{17}O$ 3–2 toward all 17 sources. The red and blue contours represent the red-shifted and blue-shifted components. The image in grey color represents the normalized SCUBA 850 μm continuum emission. The position offsets in their peak positions near the forming stars suggest that these high-velocity gases trace most likely outflows. In other words, the "board" components seen in Fig. 2.2 likely do not trace infall or rotation motions.

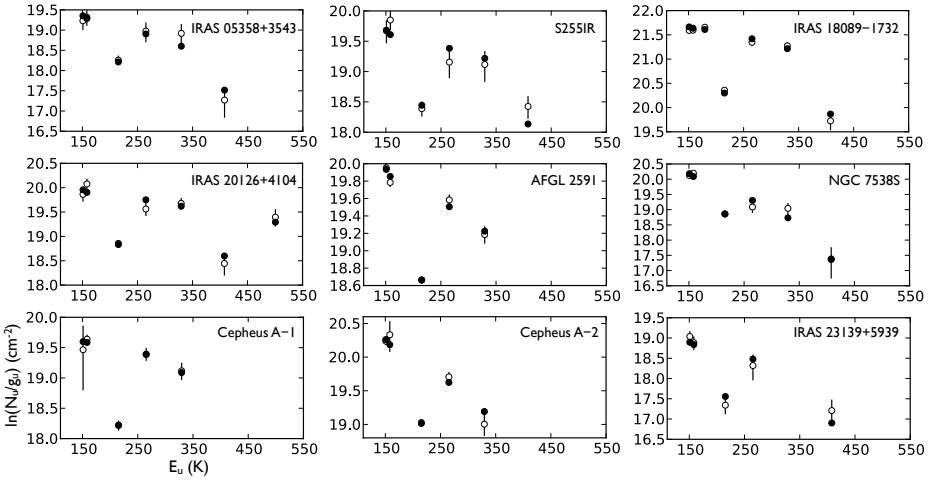

Figure 2.5 Rotation diagrams of the CH_3CN J=18–17 transitions. A set of open circles with error bars represents the observed values, while the filled circles are the best-fit RADEX model. The best-fit physical conditions are summarized in Table 2.6.

where k is Boltzmann constant, W is integrated intensity, ν is the rest frequency of transition, S is line strength, μ is electric dipole moment, g_I is spin degeneracy, and g_K is projected rotational degeneracy, is plotted versus the upper state energy $E_{\rm u}$ (Fig. 2.5). If all observed transitions are optically thin and characterized by a single excitation temperature, the points in the rotation diagram should lie on a straight line. In Fig. 2.5, the observed points are fairly scattered (especially the K = 3 and 6 transitions), suggesting that some transitions may be optically thick, and/or the excitation is not in local thermodynamic equilibrium (LTE). Therefore we do not perform a rotation diagram fit (Turner 1991) to our data. Instead, we use the code RADEX (van der Tak et al. 2007) to analyze the CH_3CN J=18–17 excitation. The code calculates the level population with the considerations of collisional and radiative excitation, and line opacities. We assume that the large velocity gradient (LVG) regime can be applied to our sources. We further assume that the source is characterized by a single kinetic temperature ($T_{\rm kin}$), a total column density ($N_{\rm mol}$), and an H_2 volume density ($n(H_2)$). We perform χ^2 optimization of a grid of models to obtain the best-fit solution to the above variables. In addition, we apply a beam filling factor (f, between 0 and 1) to scale the model intensities before calculating χ^2, assuming all transitions have the same source size. The best-fit solutions are plotted in the form of rotation diagram in Fig. 2.5 (filled circles) and summarized in Table 2.6. The χ^2 distribution of each free parameter is plotted in Fig. 2.9 and 2.10.

With the simplified "point-source" RADEX model, we obtain physical con-

ditions of each source with detections of CH_3CN J=18–17. The lower-K transitions are indeed optically thick. In general, the kinetic temperatures are all $\geq$ 80 K, suggesting that the J=18–17 transitions originate from a warm region in the star-forming core. The column densities vary between sources ($\sim 10^{15-17}$ cm^{-2}). The H_2 volume densities cannot be well constrained by our RADEX model (Fig. 2.9 and 2.10), but generally speaking the J=18–17 transitions probe a region with density greater than 10^6 cm^{-3}. This is consistent with the high critical densities required for collisional excitation of the transitions ($\sim 10^7$ cm^{-2}; Table 2.2). The observed level population may be slightly sub-thermalized. Interestingly, we find that the filling factors of all sources are very small ($\sim 10^{-4} - 10^{-3}$), corresponding to source sizes of a few $0.1''$ to $1''$. We assume a Gaussian beam (θ_b) and a Gaussian source (θ_s) to derive the source angular size ($f = \theta_s^2/(\theta_s^2 + \theta_b^2)$). A linear source size of few 100 AU to few 1000 AU is also derived. The estimation of source size is consistent with the point source structure observed in AFGL 2591 and Cepheus A (imaging observations; Sect. 2.2). With this result, we suggest that CH_3CN J=18–17 transitions trace an unresolved region toward all sources (with detections) at the $\sim 14''$ resolution of JCMT beam. The inferred source sizes, gas densities, and kinetic temperatures support the idea that CH_3CN traces warm and dense rotating structures toward massive star-forming cores (e.g., Beltrán et al. 2006; Cesaroni et al. 2006).

2.4.2 Toy models of kinematics

In this section, we analyze the observed $C^{17}O$ 3–2, $C^{34}S$ 7–6, and CH_3CN 18–17 line profiles toward our sample of massive star-forming cores through a comparison with toy radiative transfer models. We do not perform detailed radiative transfer modeling of the observed line profiles toward the individual sources because this procedure requires information from multiple transitions per molecule and knowledge of temperature/density/velocity profiles as well as chemistry. Instead, we introduce a simplified source configuration and focus on how different kinematics affect the synthetic line profiles. The aim is to have an idea on what kinematical component, such as infall, rotation, or turbulence, dominates the observed linewidth. We exclude outflow motion in the analysis due to its complexity (orientation, opening angle, chemistry, etc.). For some sources, the outflow contribution can be extracted by analyzing their observed $C^{17}O$ 3–2 line profile (Sect 2.3.2) and spatial distribution of high velocity gas (Sect. 2.3.3). We therefore focus on the narrow component only.

2.4.2.1 Model setup and model line profiles

We use the 2D radiative transfer code RATRAN (Hogerheijde & van der Tak 2000) as an engine to generate model line profiles with different kinematics.

We assume the model source is spherically symmetric with an outer boundary of $r_{\rm out}$ = 50,000 AU for $C^{17}O$ models and $r_{\rm out}$ = 5000 AU for $C^{34}S$/CH_3CN models. The use of different model source sizes follows from the very different critical densities of the molecules (Table 2.2). The assumption of spherical symmetry may not be true at small scales (few 1000 AU) due to conservation of angular momentum and subsequently the formation of disk-like structure or the formation of a small cluster. In the $\sim 14''$ JCMT beam, the substructures mentioned above are unresolved. The density and temperature profiles are chosen as $n(r) = 10^5(r/10000\ {\rm AU})^{-1.5}$ cm^{-3} and $T_{\rm kin}(r) = 100(r/10000\ {\rm AU})^{-0.5}$ K, respectively. The above physical conditions are sampled in 208 adaptive grid cells (Fig. 2.6 (a)–(d)). The enclosed gas masses within $r_{\rm out}$ = 50,000 AU and $r_{\rm out}$ = 5000 AU sampled by our model grid cells are about 54 $M_\odot$ and 1.7 $M_\odot$, respectively.

With these fixed density and temperature profiles, we consider two different velocity profiles: (1) free-fall motion ($v_{\rm ff}(r) = \sqrt{2GM_\star/r}$, where r is the distance to the central star), and (2) Keplerian rotation ($v_{\rm Kep}(R) = \sqrt{GM_\star/R}$, where R is the distance to the rotation axis). We note that these two different motions are the extreme cases for a star-forming core. In reality the gas motion in the envelope can be a mixture of infall and rotation. The stellar mass $M_\star$ is set at 8, 12, 16, 20, 30, and 40 $M_\odot$. For the Keplerian rotation models, we consider three different inclination angles (the angle between the rotation axis and the line of sight) at 15°, 45°, and 75°. The turbulent FWHM linewidths of all models are set at 1.0, 2.0, and 3.0 km s^{-1}. The fractional abundances of $C^{17}O$, $C^{34}S$, and CH_3CN are assumed to be 1×10^{-7}, 3×10^{-10}, and 3×10^{-8} respectively.

In Fig. 2.6 (e) to (g), we show the relative level population of the $C^{17}O$ J=3 level, the $C^{34}S$ J=7 level, and the CH_3CN $J_K = 18_3$ level, respectively. The models are calculated assuming a turbulent linewidth of 2.0 km s^{-1}, a stellar mass of 20 $M_\odot$, and a core with free-fall motion. The population plots are similar to those in Fig. 2.6 if the core is in Keplerian rotation. We found that $C^{17}O$ 3–2 emission traces the entire core except the very inner part, while the $C^{34}S$ 7–6 and CH_3CN 18_3–17_3 transitions originate only from the very inner part of the core at few 1000 AU scales (unresolved in $14''$ beam at a source distance of 4 kpc). The CH_3CN J=18–17 emission is more compact compared to $C^{34}S$ 7–6, consistent with its high upper level energy (215 K).

To simulate the model line profiles observed with a $14''$ beam, we assume a distance of 4 kpc. We chose this distance is because most of our sample sources are within 4 kpc (15 out of 17) and we use this distance as the reference to compare the observed line profiles with the modeled ones (See next section). In Fig. 2.7, we show a sample of $C^{17}O$ 3–2, $C^{34}S$ 7–6, and CH_3CN 18_3–17_3 line profiles with free-fall motion or Keplerian rotation (with 45° inclination) with different stellar masses and turbulent linewidths. As expected, the line profile becomes broader if turbulent linewidth and stellar mass increase. Stronger

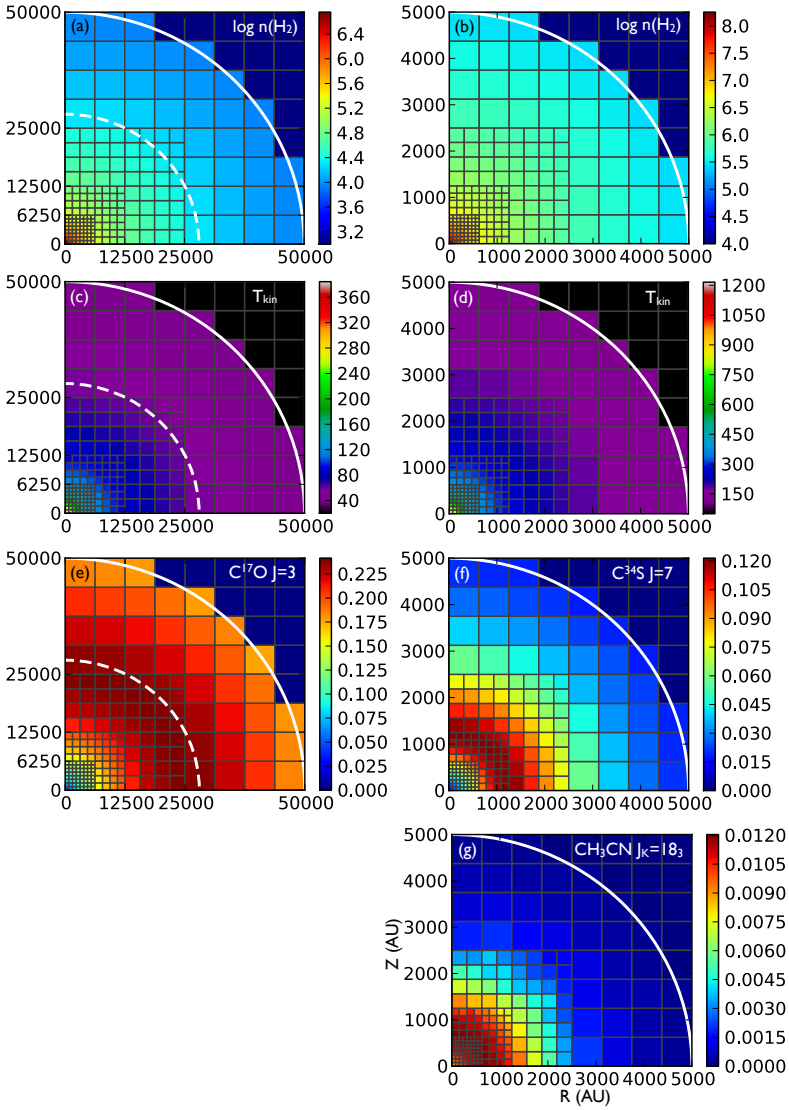

Figure 2.6 RATRAN model distributions of gas density in cm^{-3} (a)/(b), kinetic temperature in K (c)/(d), C^{17}O $J = 3$ relative population (e), C^{34}S $J = 7$ relative population (f), and CH_3CN $J_K = 18_3$ relative population (g). The relative population shown here was calculated assuming a stellar mass of 20 $M_\odot$, a turbulent linewidth of 2 km s^{-1}, and a free-fall motion. We use adaptive mesh to sample the models (grey grids). The solid line in white is the outer boundary of the model source, while the dashed line in white is the JCMT beam coverage at a source distance of 4 kpc. We use the same grid layout to sample the model but set the outer boundary to be different for C^{17}O ($r_{\rm out} = 50000$ AU), and for C^{34}S/CH_3CN ($r_{\rm out} = 5000$ AU).

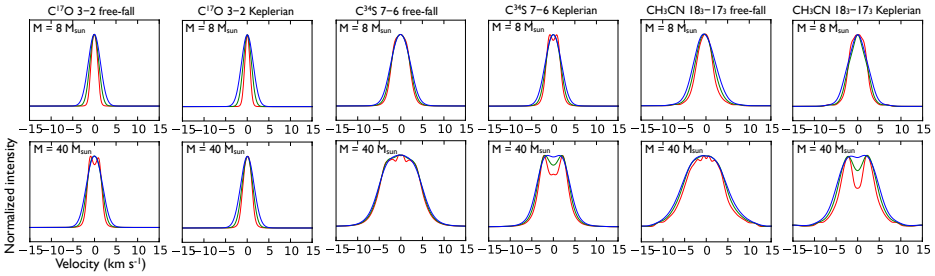

Figure 2.7 Sample RATRAN line profiles of $C^{17}O$ 3–2, $C^{34}S$ 7–6, and CH_3CN 18_3–17_3 with different stellar masses and turbulent linewidths (red: 1 km s^{-1}, green: 2 km s^{-1}, blue: 3 km s^{-1}). The inclination angle of the Keplerian rotation models is $45°$.

turbulence smears out the double-peaked signature seen in the free-fall and the Keplerian models. For lower stellar masses, the line broadening due to the increase of the turbulent linewidth is more noticeable. However, for high stellar masses, the increase in turbulence does not change the linewidth significantly, which is dominated by either the infalling motions or the rotation.

2.4.2.2 Comparison with observations

With a grid of models comprising different kinematics, stellar masses, and turbulent linewidths, we now compare the observed line FWHM linewidths with the modeled ones (Fig. 2.8). We plot the FWHM linewidth (measured from observations and models) versus the stellar mass. The stellar mass of each source in our sample is calculated based on the zero-age main-sequence luminosity listed by Mottram et al. (2011) and assuming no contribution from accretion luminosity to the total luminosity. The inferred stellar mass is therefore an upper limit of the real mass. We present the models with three different turbulent FWHM linewidths (blue: 3 km s^{-1}; green: 2 km s^{-1}; red: 1 km s^{-1}). In the plots of Keplerian models, each curve (inclination angle = $45°$) is overplotted with a colored region. The upper and lower boundaries of the colored regions represent the FWHM linewidth measured at $75°$ and $15°$, respectively.

Since all models are calculated assuming a source distance of 4 kpc, we need to consider the effect of different source distances in our sample when comparing observations with models. To check if the distance changes the linewidth significantly, we integrated over an effective linear area covered by a $14''$ beam at 4 kpc for sources within 4 kpc to derive the effective linewidth. We found that the difference between the linewidth at the real distances and at an effective 4 kpc is generally small ($\pm$0.1–0.3 km s^{-1}) in both $C^{17}O$ 3–2 and $C^{34}S$ 7–6. Therefore the difference in source distance should not be a dominant factor when

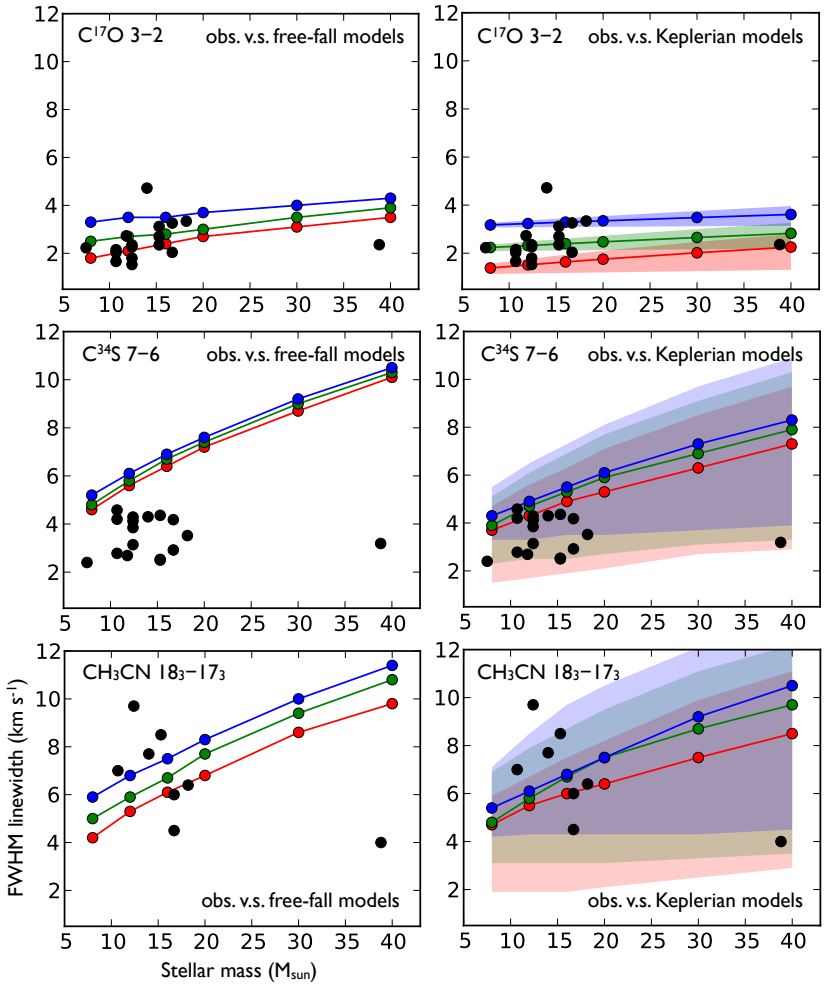

Figure 2.8 Comparison of observed FWHM linewidth with model FWHM linewidth. In all panels, the three curves represent the models with different turbulent FWHM linewidths (blue: 3 km s^{-1}; green: 2 km s^{-1}; red: 1 km s^{-1}). In the panels of Keplerian models, additional colored regions are overplotted for each curve. The upper boundary and lower boundary are the model FWHM linewidths measured at $75°$ and $15°$ inclination angles, respectively. The curve is the linewidth at $45°$ inclination. The black circles are the observed line FWHM linewidths plotted versus the inferred upper limit main-sequence masses (based on Mottram et al. (2011)).

comparing the ensemble of the observed linewidths with the models at 4 kpc.

The observed $C^{17}O$ 3–2 linewidths agree well with the models. However, as is shown in Fig. 2.8, the model linewidths do not depend strongly on the stellar mass but do reflect the adopted turbulence. This is explained by the fact that the $C^{17}O$ 3–2 emission originates from large radii, where the infall and/or rotation is small compared to the adopted turbulence of 1–3 km s^{-1}. We therefore conclude that the narrow component of $C^{17}O$ 3–2 line predominantly traces the turbulence on large scales.

For $C^{34}S$ 7–6 we find that the models do not depend strongly on the adopted turbulence but do depend on the stellar mass. This is explained by the fact that the emission originates from relatively small radii where the infalling or rotating motions are much larger than the adopted turbulence. Interestingly, the observed $C^{34}S$ 7–6 linewidths are well below the model curves. Even in the absence of turbulence, rotation or infall would generate wider lines. This could mean that the core is static, but in the light of the CH_3CN results discussed below, we prefer the interpretation that the $C^{34}S$ line originates from larger radii than suggested by our model. A flatter density profile could reproduce such behavior.

The observed CH_3CN 18_3–17_3 linewidths show a fairly large scatter but agree well in magnitude with both infalling and rotating models. Like the models for $C^{34}S$, these mostly depend on the stellar mass, indicating that in the models the emission originates from small radii. The observations and their scatter can be well explained by models with rotation where differences in inclination cause the scatter. The fact the CH_3CN shows broader lines than $C^{34}S$ in spite of similar critical densities is attributed to the larger upper-level energies (265 K v.s. 65 K, respectively), limiting the region of efficient excitation to small radii even in the presence of a flatter density profile as implied above.

In summary, we find the $C^{17}O$ 3–2 traces the turbulence on 10,000 AU scales, that $C^{34}S$ 7–6 traces turbulence on a few 1000 AU scales, and that CH_3CN 18_3–17_3 may trace rotation on $<$1000 AU scales. We confirm that this transition may indeed by an excellent tracer of disk-like structure around massive stars, but stress that detailed modeling of individual sources and high resolution observations are required to confirm this.

2.5 Discussion

2.5.1 Caveats of our qualitative comparison

In our comparison of the observed linewidth with toy radiative transfer models, there are some caveats that need to be pointed out. Firstly, we have assumed that all sources in our sample can be characterized by a spherical core with fixed temperature and density profiles regardless the central stellar mass. In reality, the temperature and density profiles may vary with respect to the stellar mass. Once

the central star becomes more massive, the surrounding core should be warmer. In addition, the temperature and density profiles should also depend on the evolutionary stages of the forming star. Different profiles could change the excitation condition significantly and hence the observed linewidth. The $C^{34}S$ results already imply that a flatter density profile than the adopted $r^{-1.5}$ powerlaw may be appropriate.

Also, we have assumed uniform turbulence in our model star-forming core regardless of stellar mass. In reality, powerful outflows and stellar radiation from the forming massive stars could provide the source of turbulence in star-forming cores. The strength of turbulence may also vary as a function of radius. If the variation of turbulence is considered in our toy models, the model linewidths change accordingly.

In future work, we will explore the caveats listed above by studying the sensitivity of the synthetic line profile to the free parameters in our model. More realistic models including both infall and rotation (Ulrich 1976) will also be generated and compared to our observations.

2.5.2 Molecular tracers of kinematics in massive star-forming cores

In this study, we use the optically thin $C^{17}O$ 3–2 and $C^{34}S$ 7–6 transitions and the optically thick CH_3CN 18–17 lines as diagnostics of kinematics of massive star-forming cores. We found that CH_3CN 18–17 is a good potential tracer of rotation in the inner core, although the Gaussian line shapes indicate that turbulence is important. We also found that $C^{34}S$ 7–6 and $C^{17}O$ 3–2 probe turbulence on a few thousand to a few 10,000 AU scales. $C^{17}O$ 3–2 also shows a broad line component (FWHM linewidth $\sim$ 3.5–9.0 km s^{-1}) which likely traces outflow activity.

As a consequence of infall onto star-forming cores, the formation of circumstellar disks and bipolar outflows provides a way to transport and release excess angular momentum of an accreting object (Shu et al. 1987). Outflows, usually observed in low-J CO transitions and SiO, toward massive star-forming regions are found to be ubiquitous as they are in dense cores forming low-mass stars (e.g, Zhang et al. 2001; Beuther et al. 2002; Klaassen & Wilson 2007). The large mass loss rates ($\sim$ few times 10^{-4} $M_\odot$ yr^{-1}) serve as an indication that the central disk-like structure should accrete gas from the envelope and transport it to the forming star at similar strength. In this study, we found that $C^{17}O$ 3–2 can trace outflows as seen in the broad line wings and the narrow component traces turbulence. In CH_3CN 18–17, we do not see large scale outflow signature in our maps. Instead, speculated from our modeling of the observed linewidth, we suggest that this line traces rotation, though small-scale ($< 14''$) outflows cannot be ruled out. From high-resolution interferometric observations, rotation signatures have been found in $C^{34}S$ and CH_3CN toward some massive star-forming

cores (e.g., Beltrán et al. 2006; Cesaroni et al. 2006). In the case of $C^{34}S$ this implies that emission from rotating regions may be a small fraction of the total line emission picked up by our single-dish measurements. We suggest that future high-resolution survey of massive star-forming cores in $C^{34}S$ and CH_3CN may help in enlarging the detection rate of massive disks. We also suggest that hot core molecules (HCOOH, CH_3CN, $HCOOCH_3$, etc.) may be good tracers of massive disks as some authors already pointed out from their high-resolution observations (e.g., Beuther et al. 2004; Wang et al. 2011).

2.6 Conclusion and future work

In this work, we observed $C^{17}O$ 3–2, $C^{34}S$ 7–6, and CH_3CN 18–17 toward 17 massive star-forming cores with the JCMT, aiming at testing what kind of kinematics these lines can trace. We found that CH_3CN 18–17 is a good potential tracer of rotation in the inner core, although the Gaussian line shapes indicate that turbulence is important. We also found that $C^{34}S$ 7–6 and $C^{17}O$ 3–2 probe turbulence on a few 1000 AU to a few 10,000 AU scales. $C^{17}O$ 3–2 also shows a broad line component which likely traces outflow activity.

In the future, we will study how different core temperature and density profiles can affect the synthetic linewidth, which will allow us to better establish the robustness of the line tracers as probes of rotation of star-forming cores. We will also construct a more realistic model including a self-consistent density and velocity profiles of a infalling and rotating star-forming core.

Acknowledgements

The research of K.-S.W. at Leiden Observatory is supported through a PhD grant from the Nederlandse Onderzoekschool voor Astronomie (NOVA). The authors thank the JCMT staff for conducting our observations. This research has made use of NASA's Astrophysics Data System Bibliographic Services.

2.7 Supplementary material

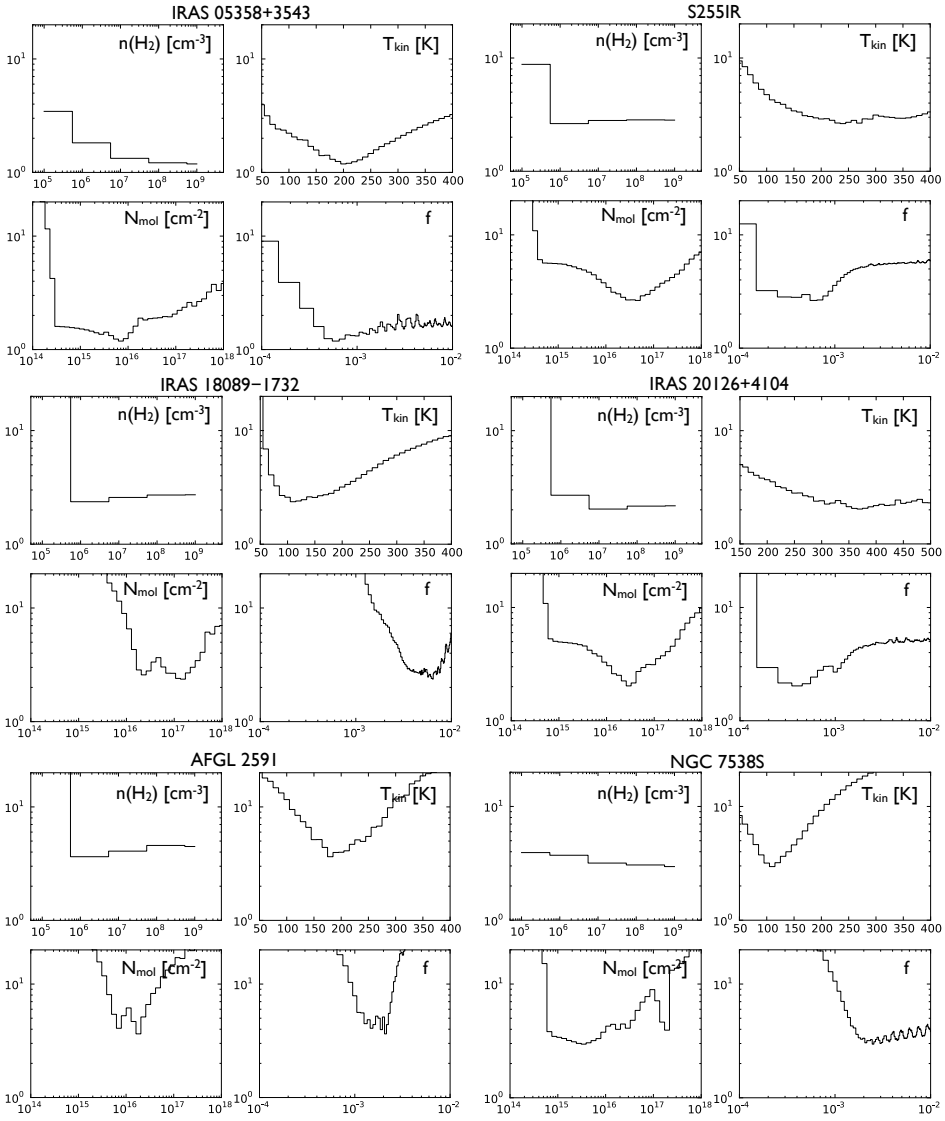

Figure 2.9 χ^2 value (y-axis of each panel) verses each free parameter in RADEX excitation analysis of CH_3CN lines. Only the lower-bound of χ^2 distribution is plotted.

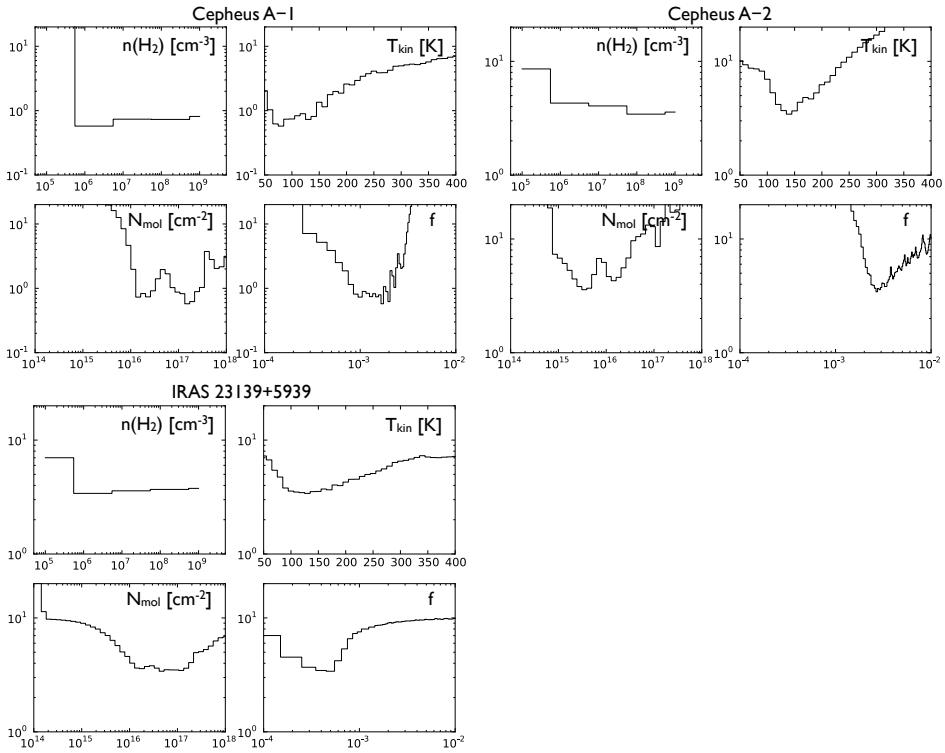

Figure 2.10 χ^2 value (y-axis of each panel) verses each free parameter in RADEX excitation analysis of CH_3CN lines. Only the lower-bound of χ^2 distribution is plotted.

Bibliography

Arce, H. G., Shepherd, D., Gueth, F., et al. 2007, Protostars and Planets V, 245

Beltrán, M. T., Cesaroni, R., Codella, C., et al. 2006, Nature, 443, 427

Beltrán, M. T., Cesaroni, R., Neri, R., et al. 2005, A&A, 435, 901

Beuther, H., Churchwell, E. B., McKee, C. F., & Tan, J. C. 2007, Protostars and Planets V, 165

Beuther, H., Hunter, T. R., Zhang, Q., et al. 2004, ApJ, 616, L23

Beuther, H., Schilke, P., Sridharan, T. K., et al. 2002, A&A, 383, 892

Birkmann, S. M., Krause, O., Hennemann, M., et al. 2007, A&A, 474, 883

Bonnell, I. A., Bate, M. R., Clarke, C. J., & Pringle, J. E. 2001, MNRAS, 323, 785

Buckle, J. V., Hills, R. E., Smith, H., et al. 2009, MNRAS, 399, 1026

Cesaroni, R., Galli, D., Lodato, G., Walmsley, C. M., & Zhang, Q. 2007, Protostars and Planets V, 197

Cesaroni, R., Galli, D., Lodato, G., Walmsley, M., & Zhang, Q. 2006, Nature, 444, 703

Di Francesco, J., Johnstone, D., Kirk, H., MacKenzie, T., & Ledwosinska, E. 2008, ApJS, 175, 277

Evans, II, N. J. 1999, ARA&A, 37, 311

Furuya, R. S., Cesaroni, R., & Shinnaga, H. 2011, A&A, 525, A72

Furuya, R. S., Cesaroni, R., Takahashi, S., et al. 2008, ApJ, 673, 363

Goldsmith, P. F. & Langer, W. D. 1999, ApJ, 517, 209

Green, S. 1986, ApJ, 309, 331

Hatchell, J., Fuller, G. A., Millar, T. J., Thompson, M. A., & Macdonald, G. H. 2000, A&A, 357, 637

Hogerheijde, M. R. & van der Tak, F. F. S. 2000, A&A, 362, 697

Isokoski, K., Bottinelli, S., & van Dishoeck, E. F. 2013, A&A, 554, A100

Klaassen, P. D. & Wilson, C. D. 2007, ApJ, 663, 1092

Klaassen, P. D. & Wilson, C. D. 2008, ApJ, 684, 1273

Krumholz, M. R., Klein, R. I., McKee, C. F., Offner, S. S. R., & Cunningham, A. J. 2009, Science, 323, 754

Krumholz, M. R., McKee, C. F., & Klein, R. I. 2005, ApJ, 618, L33
Lacy, J. H., Knacke, R., Geballe, T. R., & Tokunaga, A. T. 1994, ApJ, 428, L69
Liu, T., Wu, Y., Liu, S.-Y., et al. 2011a, ApJ, 730, 102
Liu, T., Wu, Y., Zhang, Q., et al. 2011b, ApJ, 728, 91
López-Sepulcre, A., Codella, C., Cesaroni, R., Marcelino, N., & Walmsley, C. M. 2009, A&A, 499, 811
López-Sepulcre, A., Walmsley, C. M., Cesaroni, R., et al. 2011, A&A, 526, L2
McKee, C. F. & Ostriker, E. C. 2007, ARA&A, 45, 565
McKee, C. F. & Tan, J. C. 2003, ApJ, 585, 850
Mottram, J. C., Hoare, M. G., Davies, B., et al. 2011, ApJ, 730, L33
Myers, P. C., Mardones, D., Tafalla, M., Williams, J. P., & Wilner, D. J. 1996, ApJ, 465, L133
Palla, F. & Stahler, S. W. 1993, ApJ, 418, 414
Rygl, K. L. J., Wyrowski, F., Schuller, F., & Menten, K. M. 2013, A&A, 549, A5
Sault, R. J., Teuben, P. J., & Wright, M. C. H. 1995, in Astronomical Society of the Pacific Conference Series, Vol. 77, Astronomical Data Analysis Software and Systems IV, ed. R. A. Shaw, H. E. Payne, & J. J. E. Hayes, 433
Schöier, F. L., van der Tak, F. F. S., van Dishoeck, E. F., & Black, J. H. 2005, A&A, 432, 369
Shu, F. H., Adams, F. C., & Lizano, S. 1987, ARA&A, 25, 23
Sridharan, T. K., Beuther, H., Schilke, P., Menten, K. M., & Wyrowski, F. 2002, ApJ, 566, 931
Terebey, S., Shu, F. H., & Cassen, P. 1984, ApJ, 286, 529
Torstensson, K. J. E., van der Tak, F. F. S., van Langevelde, H. J., Kristensen, L. E., & Vlemmings, W. H. T. 2011, A&A, 529, A32
Turner, B. E. 1991, ApJS, 76, 617
Turner, B. E., Chan, K.-W., Green, S., & Lubowich, D. A. 1992, ApJ, 399, 114
Ulrich, R. K. 1976, ApJ, 210, 377
van der Tak, F. F. S., Black, J. H., Schöier, F. L., Jansen, D. J., & van Dishoeck, E. F. 2007, A&A, 468, 627
van der Tak, F. F. S., van Dishoeck, E. F., Evans, II, N. J., & Blake, G. A. 2000, ApJ, 537, 283
Wang, Y., Beuther, H., Bik, A., et al. 2011, A&A, 527, A32
Wilson, T. L. & Rood, R. 1994, ARA&A, 32, 191
Wyrowski, F., Güsten, R., Menten, K. M., Wiesemeyer, H., & Klein, B. 2012, A&A, 542, L15
Yang, B., Stancil, P. C., Balakrishnan, N., & Forrey, R. C. 2010, ApJ, 718, 1062
Zhang, Q., Hunter, T. R., Brand, J., et al. 2001, ApJ, 552, L167
Zinnecker, H. & Yorke, H. W. 2007, ARA&A, 45, 481